

Long, depolarising $H\alpha$ -filament towards the Monogem ring^{*}

Wolfgang Reich¹, Patricia Reich¹ and Xiaohui Sun²

¹ Max-Planck-Institut für Radioastronomie, Auf dem Hügel 69, 53121 Bonn, Germany;
wreich@mpifr-bonn.mpg.de, preich@mpifr-bonn.mpg.de

² Department of Astronomy, Yunnan University, and Key Laboratory of Astroparticle Physics of Yunnan Province, Kunming 650091, China; *xhsun@ynu.edu.cn*

Received; accepted

ABSTRACT

Context. In soft X-rays, the Monogem ring is an object with a diameter of 25° located in the Galactic anti-centre. It is believed to be a faint, evolved, local supernova remnant. The ring is also visible in the far-ultraviolet, and a few optical filaments are related. It is not seen at radio wavelengths, as other large supernova remnants are.

Aims. We study a narrow about $4:5$ long, faint $H\alpha$ -filament, G203.7+11.5, that is seen towards the centre of the Monogem ring. It causes depolarisation and excessive Faraday rotation of radio polarisation data.

Methods. Polarisation observations at $\lambda 11$ cm and $\lambda 21$ cm with the Effelsberg 100-m telescope were analysed in addition to *WMAP* data, extragalactic rotation measures, and $H\alpha$ data. A Faraday-screen model was applied.

Results. From the analysis of the depolarisation properties of the $H\alpha$ filament, we derived a line-of-sight magnetic field, B_{\parallel} , of $26 \pm 5 \mu\text{G}$ for a distance of 300 pc and an electron density, n_e , of 1.6 cm^{-3} . The absolute largest rotation measure of G203.7+11.5 is $-86 \pm 3 \text{ rad m}^{-2}$, where the magnetic field direction has the opposite sign from the large-scale Galactic field. We estimated the average synchrotron emissivity at $\lambda 21$ cm up to 300 pc distance towards G203.7+11.5 to about $1.1 \text{ K } T_b/\text{kpc}$, which is higher than typical Milky Way values.

Conclusions. The magnetic field within G203.7+11.5 is unexpected in direction and strength. Most likely, the filament is related to the Monogem-ring shock, where interactions with ambient clouds may cause local magnetic field reversals. We confirm earlier findings of an enhanced but direction-dependent local synchrotron emissivity.

Key words. Radiation transfer – Polarisation – Radio continuum: ISM – ISM: individual objects: Monogem Ring – ISM: magnetic fields

1. Introduction

X-rays from the Monogem ring were first detected during a rocket flight in 1969 (Bunner et al. 1971). It is seen as a bright soft X-ray object with a diameter of 25° in the *ROSAT* All-sky survey (Voges et al. 1999), where its centre is at $l, b \sim 201^\circ, +12^\circ$. The Monogem ring was discussed in some detail by Plucinsky et al. (1996), who concluded that it is a large evolved supernova remnant (SNR) in the adiabatic phase of evolution that expands in a very low-density interstellar medium (ISM). More recent X-ray observations of the Monogem ring with *SUZAKU* led to a refined analysis of the SNR parameters (Knies et al. 2018).

Far-ultraviolet (FUV) emission was detected by Kim et al. (2007), where C IV and other lines indicate interaction details of the Monogem ring with the ambient ISM. Two optical filaments associated with the Monogem ring have been identified by Reimers & Wendker (1984) and by Weinberger et al. (2006). The spectra of both filaments show excitation by a slow shock, as expected from an evolved SNR. Thorsett et al. (2003) showed that the pulsar PSR B0656+14 is located close to the centre of the Monogem ring, and the authors concluded that both objects result from a supernova explosion that occurred about one hundred thousand years ago at a distance of about 300 pc.

Send offprint requests to: wreich@mpifr.de

* The FITS images of the radio maps are available in electronic form at the CDS via anonymous ftp to ...

The Monogem ring shows no radio emission, as expected for older SNRs in the metre or decimetre range, where synchrotron emission is the dominating process. This was explained by Plucinsky et al. (1996) by the unusually low ISM density. However, Vallée (1993) pointed out that the Monogem ring and similar large local features may significantly contribute to the observed rotation measure (*RM*) of extragalactic sources, which are the basis for magnetic field models of the Milky Way.

During the observations for the $\lambda 21$ cm Effelsberg Medium Latitude Survey (EMLS) (Uyaniker et al. 1998, 1999; Reich et al. 2004), we found numerous depolarised canal-like structures in the polarisation maps. For some of them, we made follow-up observations at $\lambda 11$ cm to study the origin of the canals. A prominent long canal is seen close to the direction of the centre of the Monogem ring. The filament has a clear counterpart in the all-sky $H\alpha$ map compiled by Finkbeiner (2003). Its properties are discussed in the following. We show *ROSAT* data of the Monogem ring in Fig. 1, where we indicate the position of PSR B0656+14 and the area we observed at radio frequencies.

In Sect. 2 we describe the radio and $H\alpha$ data that we used and the zero-level calibration of the $\lambda 11$ cm polarisation data. Section 3 presents the maps of our observations. A Faraday-screen analysis is given in Sect. 4. We discuss the physical properties of G203.7+11.5 in Sect. 5, where we also derive the local synchrotron emissivity in the direction of the Monogem ring. Section 6 gives a summary.

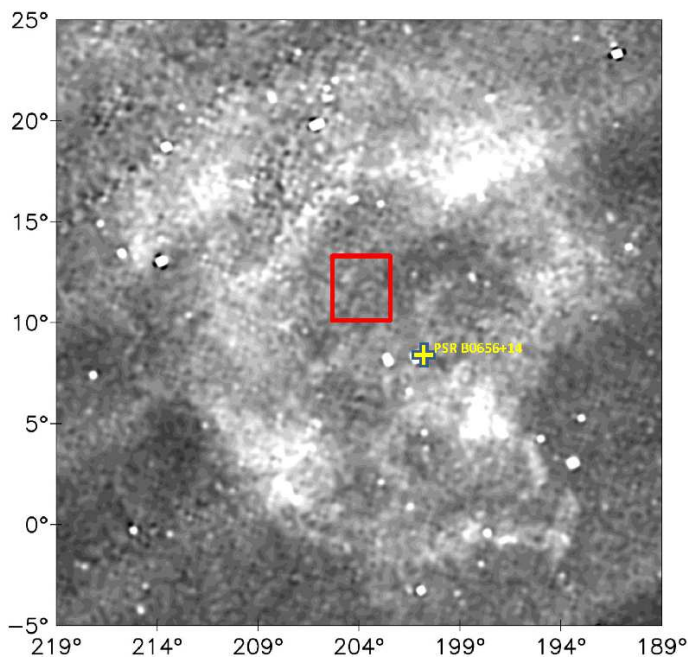


Fig. 1. Overview of the Monogem ring in soft-X-rays as observed by ROSAT (0.1- 0.4 keV band, (Voges et al. 1999)) with the related PSR B0656+14. The observed radio field is indicated.

2. Data

2.1. Effelsberg $\lambda 21$ cm data

G203.7+11.5 is visible on the EMLS $\lambda 21$ cm maps as a long, narrow polarisation depression (canal) that extends from $l, b \sim 204^\circ, +12^\circ$ to $l, b \sim 203^\circ 3', +10^\circ$. We used total-intensity and linear-polarisation data from an unpublished section of the EMLS. When completed, the EMLS will cover the northern Galactic plane $\pm 20^\circ$ in latitude at an angular resolution of $9''.4$. Table 1 lists some technical details. Missing large-scale emission components and the absolute zero-levels of the EMLS were provided by the Stockert 25-m telescope $\lambda 21$ cm total-intensity survey of the northern sky (Reich 1982; Reich & Reich 1986) and the DRAO 26-m linear-polarisation survey (Wolleben et al. 2006). Adding large-scale structures from these surveys provides an absolute zero-level for total intensities and linear polarisation. The $\lambda 21$ cm polarised-intensity (PI) map with overlaid total-intensity contours is shown in Fig. 2. PI is calculated from the observed Stokes parameter U and Q as $PI = \sqrt{U^2 + Q^2} - 1.2\sigma_{U,Q}^2$, including zero-bias correction. σ is listed in Table 1.

2.2. New Effelsberg $\lambda 11$ cm observations

Radio continuum and linear polarisation observations of G203.7+11.5 were made at $\lambda 11$ cm with the Effelsberg 100-m radio telescope. The observations started in 1997/1999 and were completed with an improved $\lambda 11$ cm receiver in 2007. The layout of the Effelsberg $\lambda 11$ cm receiving system has been described by Uyaniker et al. (2004). The receiving system available in 1997/1999 was upgraded in 2005 with new low-noise amplifiers and an eight-channel IF-polarimeter. Its channels are 10 MHz wide, and a broad-band channel provides 80 MHz bandwidth in addition, which we used when no radio interference (RFI) was visible in the observing band.

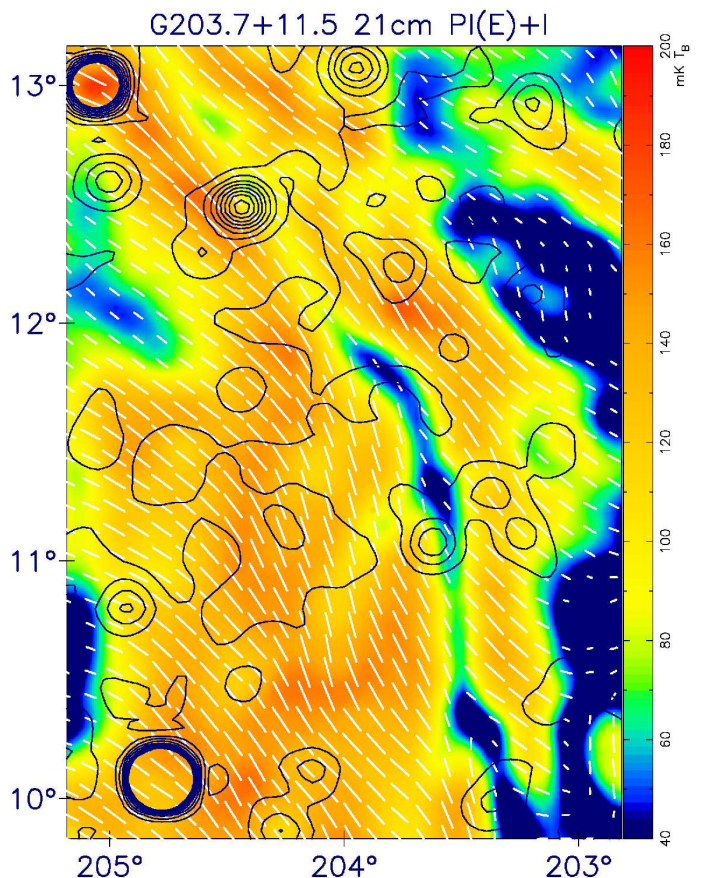


Fig. 2. Colour-coded $\lambda 21$ cm polarised emission (on an absolute zero-level) observed with the Effelsberg 100-m radio telescope. The angular resolution is $9''.4$. Overlaid contours show $\lambda 21$ cm absolute total intensities starting at 3.8 K T_b in steps of 100 mK T_b . The bars are in E-field direction, and their length is proportional to the polarised intensity.

A field of $2^\circ 33' \times 3^\circ 33'$ was mapped by raster scans in Galactic longitude and latitude direction. Altogether, eight maps in each direction were observed. However, about 50% of the observations could not or only partly be used because of RFI, solar side-lobe distortions, or bad weather. Some observational parameters are listed in Table 1. The raw data were reduced and calibrated by standard NOD2-based methods used for continuum and polarisation observations with the Effelsberg 100-m telescope (e.g. Reich et al. (1990)). We present the Effelsberg map of the $\lambda 11$ cm observations in Fig. 3.

2.3. $H\alpha$ emission

There is a clear $H\alpha$ counterpart of the polarised $\lambda 11$ cm emission in the all-sky $H\alpha$ map with $6'$ angular resolution combined by Finkbeiner (2003), which is a combination of various $H\alpha$ surveys. The $H\alpha$ map (Fig. 4) shows that the faint filament extends from $l, b \sim 204^\circ 5', +13^\circ$ to $\sim 203^\circ 1', +10^\circ$ with intensity maxima around 6 to 7 Rayleigh that become slightly fainter at its ends. The intensity gradient is moderate and increases towards the upper right area of the map. The $H\alpha$ filament exceeds the diffuse large-scale emission by about 3 to 4 Rayleigh and has a width of about $30'$ (HPBW).

Table 1. Observational parameters

Data	Effelsberg $\lambda 11$ cm	EMLS $\lambda 21$ cm
Frequency [MHz]	2639	1408
Bandwidth [MHz]	80	20
HPBW[']	4.3	9.4
Main Calibrator	3C286	3C286
Flux Density of 3C286 [Jy]	11.5	14.4
Polarisation Percentage of 3C286 [%]	9.9	9.3
Polarisation Angle of 3C286 [°]	33	32
Number of Coverages	<16	min. 1(B)+1(L)
Integration Time [s]	<16	≥ 2
r.m.s. ($I/U, Q$) [mK T_b]	4/2	15/8

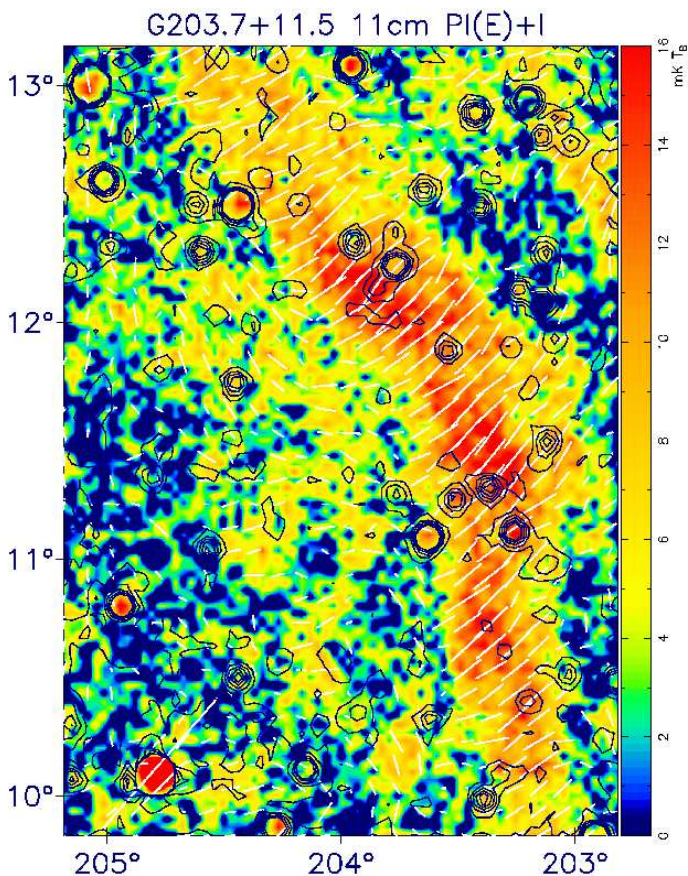


Fig. 3. As Fig. 2, but displaying $\lambda 11$ cm polarised emission as observed with the Effelsberg 100-m radio telescope without large-scale emission. The angular resolution is 4/3. Overlaid are $\lambda 11$ cm total-intensity contours starting at 10 mK T_b in steps of 20 mK T_b .

2.4. Absolute zero-level of the $\lambda 11$ cm polarisation data

Interferometric data miss short spacings, and single-dish maps are usually set to an arbitrary zero-level. As discussed by Reich (2006) and others, polarisation data without restored large-scale emission make any interpretation of polarisation features unreliable when they result from radiation transfer and not from emitting sources. Missing large-scale structures of polarisation maps from the magnetised interstellar medium will otherwise cause misinterpretations.

The observed $\lambda 11$ cm Effelsberg maps of Stokes parameters U and Q were set to zero at their boundaries and thus miss polarised emission from components exceeding about 2° to 3°

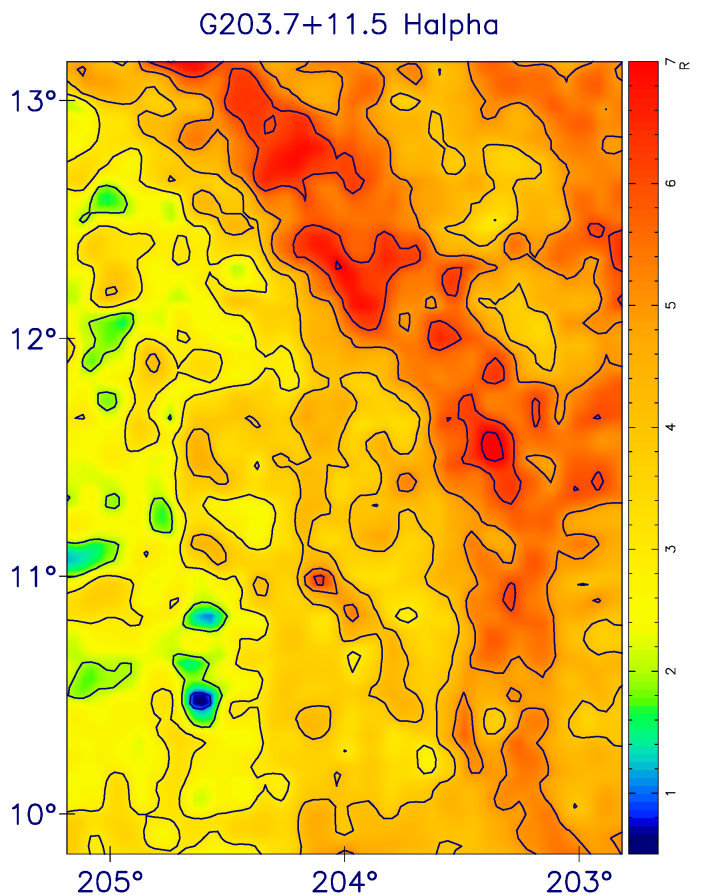


Fig. 4. $H\alpha$ emission extracted from the all-sky map of Finkbeiner (2003). Overlaid $H\alpha$ contours extend from 1 Rayleigh to 7 Rayleigh in steps of 1 Rayleigh.

in extent. The zero-level problem of single-dish telescopes was solved for the Sino-German $\lambda 6$ cm polarisation survey of the Galactic plane by Sun et al. (2007), where polarisation data on an absolute zero-level were not available, by adding scaled large-scale components from the *WMAP* K-band ($\lambda 1.3$ cm) polarisation data (Page et al. 2007). The *WMAP* polarisation data are at an absolute zero-level, as required for this purpose. This procedure assumes that Faraday rotation of the large-scale emission in the Galactic plane has a negligible influence on $\lambda 6$ cm polarisation angles PAs ($PA = \frac{1}{2} \text{atan}(U/Q)$), and thus the ratio of U and Q for large scales remains unchanged. This assumption seems to be valid for most regions of the Galactic plane at $\lambda 6$ cm, except for some emission from the innermost Galaxy. The Monogem

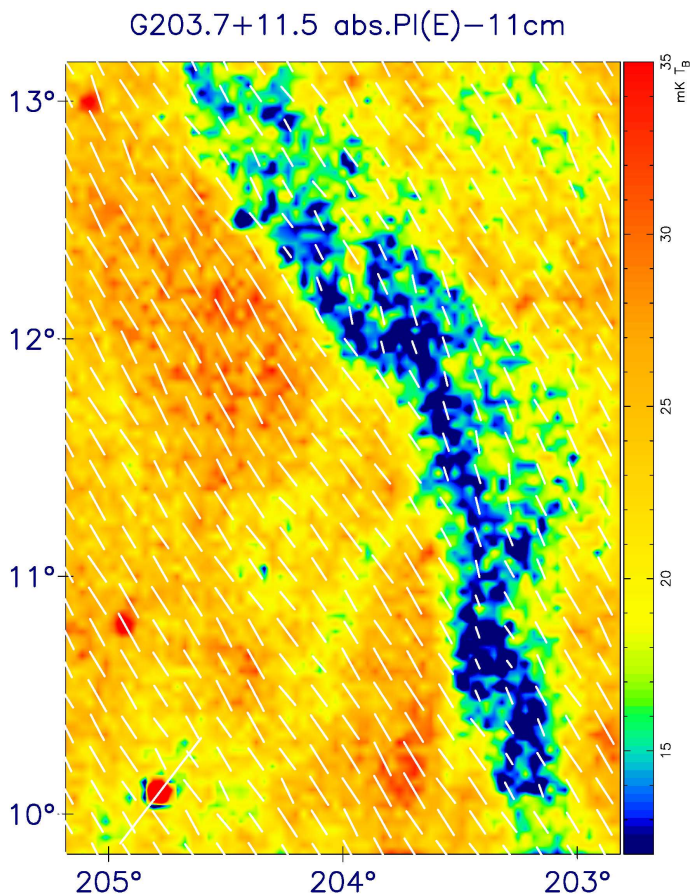


Fig. 5. Colour-coded Effelsberg $\lambda 111$ cm polarised emission as in Fig. 3 at an absolute zero-level, which was extrapolated from *WMAP* data (see Sect. 2.4).

ring is located in the Galactic anti-centre direction and well outside of the Galactic plane, so that applying the same correction method for the Effelsberg $\lambda 111$ cm polarisation data seems to be justified although the Faraday rotation is about three times higher than at $\lambda 16$ cm.

We used the $\lambda 21$ cm and the $\lambda 1.3$ cm *WMAP* absolute polarisation data (nine-year release, Hinshaw et al. (2009)) to calculate the spectral index β of the diffuse large-scale *PI* outside of the area of the thermal filament from the mean U and Q values. We found $\beta = -3.1$ ($T_b \propto \nu^{\beta}$). Between $\lambda 21$ cm and $\lambda 1.3$ cm, the mean angle difference for the large-scale emission is about $4^{\circ}4 \pm 5^{\circ}$. With $PA_{\lambda} = RM \times \lambda^2 + PA_0$, this angle difference corresponds to $RM = 1.7 \pm 1.9$ rad m^{-2} and implies a negligible correction for the $\lambda 111$ cm polarisation data. It proves that the method we used for zero-level correction can be applied to the $\lambda 111$ cm map. A recent spectral study of polarised emission observed with *PLANCK* between 30 GHz and 44 GHz by Jew & Grumitt (2019) revealed similar spectral-index values in the range $\beta = -2.99$ to $\beta = -3.12$, depending on the method that was applied.

Based on the spectral extrapolation with $\beta = -3.1$ from the $\lambda 21$ cm or the $\lambda 1.3$ cm data, we added zero-level offsets of +20.5 mK and +11.2 mK to the originally observed $\lambda 111$ cm U and Q values. The effect on the resulting *PI* emission is shown in Fig. 5. The morphology changed drastically compared to the *PI* distribution in Fig. 3, where the apparent *PI* emission along the $H\alpha$ filament is in emission, into a depression (Fig. 5). This result clearly demonstrates the importance of absolute zero-levels for mapping Galactic polarised emission and its analysis. A depres-

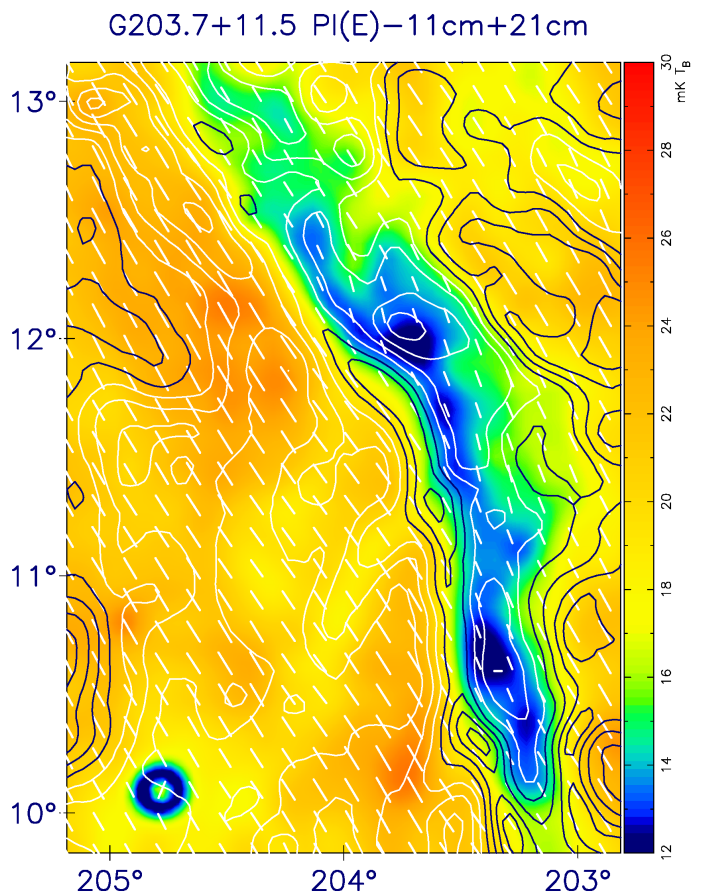


Fig. 6. Colour-coded $\lambda 111$ cm polarised intensities at 9'4 resolution, overlaid with contours of $\lambda 21$ cm polarised intensity starting at 20 mK T_b in steps of 20 mK T_b . Up to 80 mK T_b contours are shown in black. Intensities of 100 mK T_b and higher are shown by white contours. Both polarised intensities are at an absolute zero-level.

sion is expected when the $H\alpha$ filament causes sufficiently high Faraday rotation on the polarised background, which then adds to the foreground emission. When the spectral index varies by ± 0.1 , the quoted zero-level offsets for U and Q vary by 20%. This does not change the morphology, but *PI* and *PA* values are slightly different. We take the influence of offset variations into account when we discuss the Faraday-screen model in Sect. 4.

3. Total intensities and polarised emission

The $\lambda 21$ cm and $\lambda 111$ cm total-intensity contours of Fig. 2 and Fig. 3 show several compact sources in the field and small fluctuations of the diffuse emission. No significant intensity gradient or any filamentary structure is visible in total intensities. The polarisation maps at an absolute zero-level (Fig. 2 and Fig. 5), however, show filamentary features that have no counterpart in total intensities and thus result from Faraday-rotation effects along the line of sight. The narrow depolarisation canal as seen in the $\lambda 21$ cm polarised-intensity map (Fig. 2) described above is located at the gradient of the broader $\lambda 111$ cm depolarisation filament (Fig. 6) that extends from $l, b \sim 204^{\circ}5, +13^{\circ}$ to $l, b \sim 203^{\circ}1, +10^{\circ}$, which itself coincides very well with the faint $H\alpha$ filament (Fig. 4).

4. Faraday-screen model for G203.7+11.5

Sun et al. (2007) have described a method for calculating the properties of a discrete Faraday screen located somewhere along the line of sight. The modified polarised emission PI_{on} in the direction of the Faraday screen (on-position) is compared with the emission outside of the screen PI_{off} (off-position). In addition, the difference of the polarisation angles $PA_{\text{on}} - PA_{\text{off}}$ is required. The parameter c is the ratio $PI_{\text{fg}}/(PI_{\text{fg}} + PI_{\text{bg}})$, where fg and bg indicate the polarised foreground and background components, and ψ_s is the angle rotation caused by the Faraday screen. The parameter f describes the depolarisation of the Faraday screen, where 1 stands for no and 0 for total depolarisation,

$$\begin{cases} \frac{PI_{\text{on}}}{PI_{\text{off}}} = \sqrt{f^2(1-c)^2 + c^2 + 2fc(1-c)\cos 2\psi_s}, \\ PA_{\text{on}} - PA_{\text{off}} = \frac{1}{2} \arctan\left(\frac{f(1-c)\sin 2\psi_s}{c + f(1-c)\cos 2\psi_s}\right). \end{cases} \quad (1)$$

For G203.7+11.5, PA_{off} is not around zero, as is typical of PAs in the Galactic plane (Sun et al. 2007), but at about 20° , which is an offset to be subtracted from the PA map, so that Eq. 1 can be directly applied. At $\lambda 11$ cm, we found for the two required observables $PI_{\text{on}}/PI_{\text{off}}$ around 0.5 with variations, where the depolarisation maximum at $l, b \sim 203.7, +11.9$ was used for PI_{on} . We measured for $PA_{\text{on}} - PA_{\text{off}} \sim -15^\circ$ to $\sim -20^\circ$. $PI_{\text{on}}/PI_{\text{off}}$ increases at the gradients of the filament.

There are considerable fluctuations in PI and PA . They prevent a very precise estimate of the differences between on- and off-positions that indicate that the physical properties within the filament vary. In the following, we therefore calculate representative parameters. Based on Eq. 1, we obtained an angle rotation caused by the filament in the range of $\psi_s \sim -62^\circ$ to $\sim -66^\circ$ for $f = 1$. Then c is calculated as $c = 0.63 \pm 0.03$, which is the portion of the foreground polarised emission. For a wavelength of $\lambda 11$ cm, the corresponding RM is -86 ± 3 rad m^{-2} . When the internal depolarisation increases, c and/or parameter f decrease to $c = 0.61 \pm 0.03$ for $f = 0.9$ and $c = 0.58 \pm 0.03$ for $f = 0.8$, where the corresponding RM changes slightly to -82 ± 3 rad m^{-2} .

When we take the spectral uncertainties of $\Delta\beta \pm 0.1$ into account when we calculate the U and Q offsets at $\lambda 11$ cm, we see almost no effect on the angle differences $PA_{\text{on}} - PA_{\text{off}}$, but the ratio $PI_{\text{on}}/PI_{\text{off}}$ changes from about 0.5 for a spectral index of $\beta = -3.1$ to about 0.6 or 0.4 in the case of a steeper or a flatter spectrum, respectively. The corresponding foreground portions c do not change, but the RM values are then calculated as $RM = -96 \pm 2$ rad m^{-2} for $\beta = -3.2$ and $RM = -76 \pm 2$ rad m^{-2} for $\beta = -3.0$.

With decreasing depolarisation at the gradients of the filament, the absolute RM values will also decrease and are expected to affect the $\lambda 21$ cm data, where the maximum depolarisation is expected at about ± 35 rad m^{-2} , corresponding to an angle rotation of $\pm 90^\circ$ of the polarised background. Figure 6 shows that the narrow depolarisation canal runs parallel along the eastern gradient of the $\lambda 11$ cm depolarised filament. The RM value of the $\lambda 21$ cm canal of around -35 rad m^{-2} at the outer gradient of the filament is as expected, when the high absolute RM values decrease and match the low RM of the diffuse offset-emission. Along the $\lambda 11$ cm depolarised filament, the $\lambda 21$ cm PI is at a similar level compared to the off-area, which implies that the depolarisation factor f must be close to 1. The depolarisation from the Faraday screen is low and the assumption of $f = 0.8$ we quoted above seems to be a lower limit.

The slope of the PI gradients of the filament towards longer and lower Galactic longitudes are different, as can be clearly seen in the $\lambda 11$ cm PI map at 9.4 resolution in Fig. 6. The $\lambda 21$ cm canal is visible at the steeper gradient, but on the other side of the filament, there is a more extended PI minimum, which is expected from the shallow $\lambda 11$ cm PI and RM gradients, which cannot be clearly separated from the general PI fluctuations in this area. Thus the maximum depolarisation at around -35 rad m^{-2} is smoothed out.

5. Discussion

5.1. Thermal filament

To calculate the physical parameters of G203.7+11.5, we have to know its distance, size, and the electron temperature of the thermal gas. We can only make estimates of these parameters, which is reflected in the result. We assume that G203.7+11.5 is located at the distance of the Monogem ring, which is about 300 pc. The filament extends slightly to the north and south of the area shown in Fig. 4 as seen in the Finkbeiner (2003) $H\alpha$ map. Figure 4 corresponds to the area of the $\lambda 11$ cm observations. We estimated a total projected length of the filament of about 4.5 , which corresponds to 24 pc. However, the apparent size of the Monogem ring is about 25° , which means a diameter of about 130 pc if it is symmetric in 3D. If the G203.7+11.5 filament is not located near the Monogem ring centre, as suggested by its coordinates, but instead in the SNR shell, its distance then is about 235 pc or 365 pc. Its projected length in that case is about 19 pc or 29 pc, respectively.

The depolarising $H\alpha$ filament has no counterpart in total intensities, which means that the thermal emission must be very low. From the $H\alpha$ excess, $I_{H\alpha}$, of 3 to 4 Rayleigh, we may calculate the emission measure $EM[\text{pc cm}^{-6}]$ from Eq. 2, where T_4 is the electron temperature in units of 10^4 K. An $E(B - V)$ extinction correction in the direction of G203.7+11.5 raises EM by about 2% (Green et al. 2019) and can be disregarded in view of all other uncertainties,

$$EM = 2.75 T_4^{0.9} I_{H\alpha} \exp[2.44E(B - V)]. \quad (2)$$

The range of EM values in the central area of the filament is between 3.6 and 11 pc cm^{-6} for electron temperatures of 4 000 K and 10 000 K and $H\alpha$ intensities of 3 to 4 Rayleigh. We adopt an EM of 7 pc cm^{-6} in the following.

The width of the depolarising filament is about $30'$, which corresponds to 2.6 pc for a distance of 300 pc. For a cylindrical morphology, we obtain the same size L along the line of sight, but if G203.7+11.5 is a sheet-like structure seen edge-on, L may be larger. In the following, we assume the cylindrical case, which means $L = 2.6$ pc. With $EM [\text{pc cm}^{-6}] = n_e^2 [\text{cm}^{-6}] \times L [\text{pc}]$, the average electron density n_e is about 1.6 cm^{-3} for $EM = 7$ pc cm^{-6} . As discussed above, with the range of possible distances of 235 pc to 365 pc and the range of EM as a function of the electron temperature, we calculated n_e between 1.1 cm^{-3} and 2.3 cm^{-3} . However, for a clumpy thermal gas, the influence of the filling-factor f_{n_e} for n_e has to be taken into account. n_e depends on f_{n_e} as

$$n_e = \sqrt{\frac{EM}{f_{n_e} L}} \text{ cm}^{-3}. \quad (3)$$

Thus the electron density scales with the filling factor f_{n_e} as $1/\sqrt{f_{n_e}}$. It is unclear what a reasonable filling factor for G203.7+11.5 might be. In any case, values of f_{n_e} below 1 will increase n_e . Recent discussions of the filling factor were reported by Harvey-Smith et al. (2011) for H II-regions and by Gao et al. (2015) for the W4 Super-Bubble.

5.2. Magnetic field strength and pressure of G203.7+11.5

From the Faraday-screen model, we derived an RM of about -86 rad m^{-2} for the central part of G203.7+11.5. RM depends on the regular magnetic field strength along the line of sight, the electron density, and the thickness L of the filament as $RM = 0.81 n_e [\text{cm}^{-3}] B_{\parallel} [\mu\text{G}] L [\text{pc}]$. We calculated a magnetic field strength along the line of sight of about $26 \mu\text{G}$ with an uncertainty of about 20%. $26 \mu\text{G}$ is a lower limit because the orientation of the filament is most likely inclined with respect to the line of sight. A filling factor f_{n_e} that is most likely below 1 will increase B_{\parallel} by $B_{\parallel}/\sqrt{f_{n_e}}$. This high magnetic field strength largely exceeds that of the local Galactic magnetic field in the ISM in any case. This local Galactic magnetic field is typically a few μG , see for example Sun et al. (2008), Sun & Reich (2010), Ferrière (2011), Van Eck et al. (2011), and Jansson & Farrar (2012), by an order of magnitude, but is not unusual for the magnetic field strength expected in SNR shock fronts. Beyond the compression of the ambient Galactic magnetic field in the adiabatic SNR expansion phase by a factor of four, further magnetic field amplification effects may increase the magnetic field strength in SNR shock fronts up to $100 \mu\text{G}$ or more, see for example Reynolds et al. (2012) and Dubner & Giacani (2015).

The magnetic field strength in thermal filaments traced by H α emission is not known, but may be compared with filaments found for other Faraday screens. The study of magnetic fields of large H II regions based on RM s of extragalactic sources by Harvey-Smith et al. (2011) revealed values of the regular magnetic field component along the line of sight, B_{\parallel} , of between 2 and $6 \mu\text{G}$. This clearly is lower than the values we found for G203.7+11.5 and similar to Galactic magnetic field strengths observed in the disc.

Several Faraday screens were detected and discussed in the $\lambda 6 \text{ cm}$ Urumqi survey publications by Sun et al. (2007), Sun et al. (2011), Gao et al. (2010), and Xiao et al. (2009). High RM values were found for some H II regions, and in particular, from a few nearly spherical Faraday screens with sizes of up to several degrees. For most of these Faraday screens, the thermal electron density must be very low because the thermal emission is not visible in H α , and moreover, its radio continuum emission is too faint to be detected. Thus, the electron density could not be precisely determined and just lower limits for B_{\parallel} can be quoted, which reach values up to $10 \mu\text{G}$.

From a Faraday-screen analysis of the large W4 Super-Bubble, Gao et al. (2015) derived B_{\parallel} of $5 \mu\text{G}$ and estimated that the total magnetic field strength will exceed $12 \mu\text{G}$ when its geometry is taken into account. Wolleben & Reich (2004) found excessive Faraday rotation towards the ionised rims of some local Taurus molecular clouds and derived values for B_{\parallel} that exceed $20 \mu\text{G}$. The last two results for B_{\parallel} are close to what we found for G203.7+11.5. All Faraday-screen results, with the exception of those for H II regions, indicate regions or objects in the Galaxy with a significantly enhanced regular magnetic field strength when compared to typical Galactic values. In most cases, the origin is not clear, although for G203.7+11.5, the old

SNR shock-front of the Monogem ring seems to be a good candidate for having caused its strong magnetic field.

We calculated the magnetic pressure $P_{\text{mag}} = B_{\text{tot}}^2/8\pi$ for G203.7+11.5 as $P_{\text{mag}} = 2.7 \pm 0.5 \times 10^{-11} \text{ dyn cm}^{-2}$. The thermal pressure $P_{\text{ther}} = 2n_0kT_e$, where $n_0 = n_e$, in the case of total ionisation, and T_e is taken as 7000 K . We determined $P_{\text{ther}} = 3.1 \pm 1.2 \times 10^{-12} \text{ dyn cm}^{-2}$. Clearly, the magnetic pressure largely exceeds the thermal pressure and thus determines the shape and evolution of G203.7+11.5.

5.3. RM s of extragalactic sources and pulsars compared to the RM of G203.7+11.5

RM s of extragalactic sources in the G203.7+11.5 area were selected from the catalogue by Xu & Han (2014). In general, the RM s in the field are positive. Seven listed RM s are in the range $+72$ to $+100 \text{ rad m}^{-2}$. For the source at $l, b = 204^{\circ}8, 10^{\circ}1$, four RM s with $+7.0, +7.0, -7.7$ and -74.4 rad m^{-2} were listed, and the source at $l, b = 205^{\circ}1, 12^{\circ}98$ has $RM = +3.5 \text{ rad m}^{-2}$. However, these two sources have the largest distances from the map centre, so that most of the sources probably indicate that the large-scale magnetic field direction points towards us. The nearby pulsar PSR B0656+14 in the centre of the Monogem ring also has a positive but lower RM of $RM = +22.73 \text{ rad m}^{-2}$ (Sobey et al. 2019). Vallée et al. (1984) have modelled the RM distribution of the Monogem ring. They calculated a positive RM excess for a thick-shell object when compared with its surroundings. The RM value we found above from comparing the diffuse polarised emission at $\lambda 21 \text{ cm}$ and at $\lambda 1.3 \text{ cm}$ (K band) of about $RM = 1.7 \pm 1.9 \text{ rad m}^{-2}$ is much lower and indicates that very local diffuse synchrotron emission dominates. Thus, the RM s of extragalactic sources in general trace the magnetic field beyond the Monogem ring.

5.4. Origin of the magnetic field of G203.7+11.5

The G203.7+11.5 filament has an RM with a negative sign, and thus its magnetic field points in the opposite direction compared to the large-scale Galactic field traced by extragalactic sources. This means that the magnetic field of G203.7+11.5 does not result from a simple compression of the large-scale field. Shock-excited optical filaments in the Monogem area have been identified previously, and G203.7+11.5 may have the same origin, although optical spectra to prove its shock excitation are missing so far. The opposite magnetic field direction may result from instabilities that arise from the interaction of the SNR shell with interstellar clouds or from the reverse-shock interaction with material from the SN explosion if the filament is located close to the centre of the Monogem ring. Investigations of Rayleigh-Taylor instabilities by Jun et al. (1995) showed that filaments that lie orthogonal to the direction of the expanding shock-wave may be formed in this way, and magnetic fields will also be amplified by this process. It is important to find signs of shock excitation for G203.7+11.5, which will strongly support the suggested association with the Monogem ring from the present study.

5.5. Local synchrotron emissivity

We can use the separation of the foreground and background polarised emission to constrain the local synchrotron emissivity in the direction of the Monogem ring. Its small distance allows us to check previous claims of a local excess of synchrotron emissivity (Fleishman & Tokarev 1995; Wolleben & Reich 2004). The

origin of the excess is not understood, in particular if it is caused by an enhancement of the local cosmic-ray electron density or by a stronger magnetic field, when compared to more distant emissivity values. The 3D structure of the local excess is not known either, but more data from different directions will provide key information to determine its location.

We calculated the $\lambda 21$ cm synchrotron emissivity up to the 300 pc distance of G203.7+11.5 in the following way: The percentage of polarised foreground emission at $\lambda 11$ cm was determined from the Faraday-screen model to be about 63% of the total polarised emission. We assumed the same percentage at $\lambda 21$ cm, which gives about 70 mK T_b polarised foreground emission. For the maximum possible degree of polarisation of 70%, the total intensity is about 100 mK T_b or 330 mK T_b /kpc. A more realistic polarisation of 20% increases the intensity to about 350 mK T_b or 1.1 K T_b /kpc. The total-intensity emission along the line of sight at $\lambda 21$ cm is about 0.7 K T_b and the polarisation is about 16%, so that the assumption of 20% polarised emission for the local emission seems realistic. The value of 1.1 K T_b /kpc is below the value of 1.7 K T_b /kpc derived by Wolleben & Reich (2004) for the foreground synchrotron emission based on Faraday-screen effects at the rims of the local Taurus molecular clouds at a distance of 140pc, but confirms that the local synchrotron emissivity is higher than more distant Galactic values. Wolleben & Reich (2004) have discussed available Galactic synchrotron emissivity data, which span a range from 0.14 K T_b to 0.9 K T_b at $\lambda 21$ cm. The recent study of low-frequency absorption data from H II regions by Polderman et al. (2019) confirmed an increased local synchrotron emissivity.

6. Summary

Radio continuum and polarisation observations at $\lambda 11$ cm and $\lambda 21$ cm were used to study the physical properties and the magnetic field of the thermal filament G203.7+11.5. G203.7+11.5 acts as a Faraday screen and is most likely related to the Monogem ring, which is classified as an evolved SNR. For a distance of about 300 pc and an electron density of $1.6 \pm 0.6 \text{ cm}^{-3}$, we found a regular magnetic field component along the line of sight of about $26 \pm 5 \mu\text{G}$, which is a lower limit for the total regular field in the filament. The resulting RM of $-86 \pm 3 \text{ rad m}^{-2}$ is similar to the RM s of extragalactic sources observed in this direction, but with an opposite sign. The magnetic field direction of G203.7+11.5 and its unusual strength most likely originate in shock interaction of the Monogem ring with clumpy interstellar material, where instabilities cause locally enhanced magnetic fields.

Acknowledgements. This research is based on observations with the Effelsberg 100-m telescope of the MPIfR, Bonn. X.S. is supported by the National Natural Science Foundation of China (Grant No. 11763008).

References

- Bunner, A. N., Coleman, P. L., Kraushaar, W. L., & McCammon, D. 1971, *ApJ*, 167, L3
- Dubner, G. & Giacani, E. 2015, *A&A Rev.*, 23, 3
- Ferrière, K. 2011, *Mem. Soc. Astron. Italiana*, 82, 824
- Finkbeiner, D. P. 2003, *ApJS*, 146, 407
- Fleishman, G. D. & Tokarev, Y. V. 1995, *A&A*, 293, 565
- Gao, X. Y., Reich, W., Han, J. L., et al. 2010, *A&A*, 515, A64
- Gao, X. Y., Reich, W., Reich, P., Han, J. L., & Kothes, R. 2015, *A&A*, 578, A24
- Green, G. M., Schlafly, E., Zucker, C., Speagle, J. S., & Finkbeiner, D. 2019, *ApJ*, 887, 93
- Harvey-Smith, L., Madsen, G. J., & Gaensler, B. M. 2011, *ApJ*, 736, 83
- Hinshaw, G., Weiland, J. L., Hill, R. S., et al. 2009, *ApJS*, 180, 225
- Jansson, R. & Farrar, G. R. 2012, *ApJ*, 757, 14
- Jew, L. & Grumitt, R. 2019, arXiv e-prints, arXiv:1907.11426
- Jun, B.-I., Norman, M. L., & Stone, J. M. 1995, *ApJ*, 453, 332
- Kim, I.-J., Min, K.-W., Seon, K.-I., et al. 2007, *ApJ*, 665, L139
- Knies, J. R., Sasaki, M., & Plucinsky, P. P. 2018, *MNRAS*, 477, 4414
- Page, L., Hinshaw, G., Komatsu, E., et al. 2007, *ApJS*, 170, 335
- Plucinsky, P. P., Snowden, S. L., Aschenbach, B., et al. 1996, *ApJ*, 463, 224
- Polderman, I. M., Haverkorn, M., Jaffe, T. R., & Alves, M. I. R. 2019, *A&A*, 621, A127
- Reich, P. & Reich, W. 1986, *A&AS*, 63, 205
- Reich, W. 1982, *A&AS*, 48, 219
- Reich, W. 2006, in *Cosmic Polarization*, ed. R. Fabbri (Research signpost), 91
- Reich, W., Fürst, E., Reich, P., & Reif, K. 1990, *A&AS*, 85, 633
- Reich, W., Fürst, E., Reich, P., et al. 2004, in *The Magnetized Interstellar Medium*, ed. B. Uyaniker, W. Reich, & R. Wielebinski (Copernicus GmbH, Katlenburg-Lindau), 45
- Reimers, D. & Wendker, H. J. 1984, *A&A*, 131, 375
- Reynolds, S. P., Gaensler, B. M., & Bocchino, F. 2012, *Space Sci. Rev.*, 166, 231
- Sobey, C., Bilous, A. V., Griebmeier, J. M., et al. 2019, *MNRAS*, 484, 3646
- Sun, X. H., Han, J. L., Reich, W., et al. 2007, *A&A*, 463, 993
- Sun, X. H. & Reich, W. 2010, *Research in Astronomy and Astrophysics*, 10, 1287
- Sun, X. H., Reich, W., Han, J. L., et al. 2011, *A&A*, 527, A74
- Sun, X. H., Reich, W., Waelkens, A., & Enßlin, T. A. 2008, *A&A*, 477, 573
- Thorsett, S. E., Benjamin, R. A., Brisken, W. F., Golden, A., & Goss, W. M. 2003, *ApJ*, 592, L71
- Uyaniker, B., Fürst, E., Reich, W., Reich, P., & Wielebinski, R. 1998, *A&AS*, 132, 401
- Uyaniker, B., Fürst, E., Reich, W., Reich, P., & Wielebinski, R. 1999, *A&AS*, 138, 31
- Uyaniker, B., Reich, W., Yar, A., & Fürst, E. 2004, *A&A*, 426, 909
- Vallée, J. P. 1993, *ApJ*, 419, 670
- Vallée, J. P., Broten, N. W., & MacLeod, J. M. 1984, *A&A*, 134, 199
- Van Eck, C. L., Brown, J. C., Stil, J. M., et al. 2011, *ApJ*, 728, 97
- Voges, W., Aschenbach, B., Boller, T., et al. 1999, *A&A*, 349, 389
- Weinberger, R., Temporal, S., & Stecklum, B. 2006, *A&A*, 448, 1095
- Wolleben, M., Landecker, T. L., Reich, W., & Wielebinski, R. 2006, *A&A*, 448, 411
- Wolleben, M. & Reich, W. 2004, *A&A*, 427, 537
- Xiao, L., Reich, W., Fürst, E., & Han, J. L. 2009, *A&A*, 503, 827
- Xu, J. & Han, J.-L. 2014, *Research in Astronomy and Astrophysics*, 14, 942